Computational Electromagnetic Field Calculation by means of Finite Integration Technique (FIT) and/or Method of Moment (MoM)

A.Ciccomancini Scogna[#], M. Strydom[#]

[#] CST of America Inc, 10 Laurel Avenue, Suite 300, Wellesley Hills (MA) 02481 USA - antonio.ciccomancini@cst.com , marli.strydom@cst.com

Abstract – The present paper offers an overview of two computational electromagnetic methods: Finite Integration Technique (FIT) and Method of Moments (MoM) with the enhancement of the Multilevel Fast Multipole Method (MLFMM). Both methods are the solution in the integral form of Maxwell equations, with both methods having their specific advantages. A number of examples, covering different fields of applications ranging from high speed printed circuit boards (PCBs), packages and electromagnetic bandgap structures (EBGs) to antennas and radar-cross-section (RCS) problem-types are analyzed and validated by means of measured data, other numerical techniques and/or analytical formulations. It is illustrated how FIT can be implemented with both hexahedral and tetrahedral meshes, offering in this way the possibility to study the same problem with two different approaches and validating therefore the numerically calculated results. It is finally discussed how MoM in combination with the MLFMM is well suitable for the solution of large problems (30-50λ) due to the linear scalability O (NlogN) of the matrix calculation.

1. Introduction

Efficient and accurate simulations of electromagnetic fields are more important than ever in the industrial construction and design optimization of electromagnetic technical devices. Increasingly, topics such as electromagnetic compatibility (EMC), electromagnetic interference (EMI), as well as the related signal integrity (SI) and power integrity (PI) become important due to the ongoing miniaturization and higher operating frequencies of devices. In many cases, analytical approaches and/or circuit level simulations can not predict sufficiently the functionality of the electrical devices, and full wave simulations need to be used.

Stringent time-to-market requirements mean that there is no time for time consuming prototyping activities in which measurements can be carried out in proper facilities. Consequently, computation of the electromagnetic (EM) behaviour of a circuit has replaced direct measurements in the prototyping phase.

Numerical techniques generally require more computation effort than analytical techniques or expert systems, since they attempt to solve fundamental field equations directly, subject to the boundary constraints posed by the geometry. Without making a priori assumptions about which field interactions are most significant, numerical techniques analyze the entire geometry provided as input.

In the *full-wave* (field based) approach, Maxwell's full electrodynamics equations are solved without any simplification such as in the quasi-static approach. Discretization of Maxwell's equations is applied in the region of interest to find the approximate electric (*E*) and magnetic (*H*) field components at various locations in the system.
Once the approximate field components are obtained, equivalent current and voltage can be simply calculated by means of the following equations:

$$V_{ba} = -\int_a^b \overline{E} \times dl$$
$$I = \int_c \overline{H} \times dl \qquad (1)$$

In (1) *c* denotes a closed path encircling the conductor with electric current flowing within it, while *a* and *b* denote two different points on the conducting structures of the model.
Note that both the relations (1) are only accurate where quasi-static mode and quasi-transverse electric magnetic (TEM) propagation mode is valid in the system.
For very high frequency systems we usually do away with the notion of voltage and current, it is simply the interaction of the *E* and *H* fields in the system and the physics of each component that determines the outcome.
A number of different numerical techniques for solving electromagnetic problems are available and each numerical technique is usually well-suited for the analysis of a particular type of problem. In this work two numerical methods are discussed: FIT and MoM; these methods are both implemented in the commercial software CST Studio Suite 2006B™
The paper is organized as follows: in the next section an introduction of the FIT is provided along with an overview of different applications resolved in time and/or frequency domain. Next the MoM and the MLFMM are briefly described and applications are presented as well. Finally some concluding remarks pointing out the advantages/disadvantages of both numerical methods are discussed.

2. The Finite Integration Technique (FIT)

Finite Integration Technique (FIT) was first proposed by T. Weiland [1-2]. This numerical method discretizes the integral form of Maxwell's equations and provides a universal spatial discretization scheme, applicable to various electromagnetic problems, ranging from static field calculations to high frequency applications in time or frequency domain.

$$\int_S \vec{E} \bullet \vec{n} dS = \frac{1}{\varepsilon_0} \int \rho dV \qquad (2)$$

$$\oint_C \vec{E} \bullet d\vec{C} = -\frac{d}{dt} \int_S \vec{B} \bullet \vec{n} dS \qquad (3)$$

$$\int_S \vec{B} \bullet \vec{n} dS = 0 \qquad (4)$$

$$\oint_C \vec{B} \bullet d\vec{C} = \mu_0 I + \mu_0 \varepsilon_0 \int_S \frac{\partial}{\partial t} \vec{E} \bullet \vec{n} dS \tag{5}$$

In order to numerically solve Maxwell's equations a finite calculation domain is defined, enclosing the considered application problem. By creating a suitable mesh system, this domain is split up into several small cuboids, so-called grid cells. The spatial discretization of Maxwell's equations is finally performed on two orthogonal grid systems, where the new degrees of freedom are introduced as integral values as well.
Referring to Figure 1a, the electric grid voltages **e** and magnetic facet fluxes **b** are allocated on the primary grid *G* and the dielectric facet fluxes **d** as well as the magnetic grid voltages **h** on the dual grid $\tilde{G}$ (indicated by the tilde).

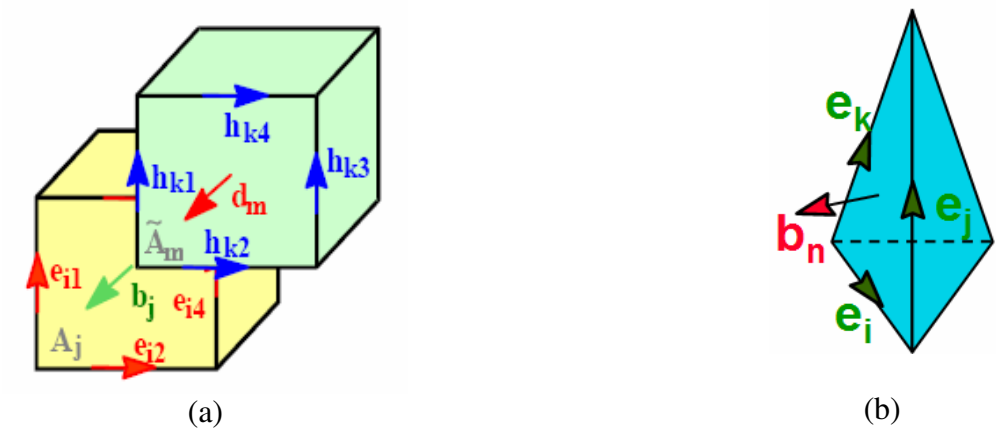

(a) (b)

Figure1 – a): Hexahedral mesh with dual discretization grid for electric and magnetic fluxes, b): Tetrahedral mesh representation for frequency domain solver.

As an example, consider Faraday's law. The closed integral on the equation (3) can be rewritten as a sum of four grid voltages without introducing any supplementary errors (6-7). Consequently, the time derivative of the magnetic flux defined on the enclosed primary cell facet represents the right-hand side of the equation (3).
By repeating this procedure for all available cell facets, the calculation rule can be summarized in a matrix formulation, introducing the topological matrix **C** as the discrete equivalent of the analytical curl operator (8)

$$\oint_{\partial A_n} \vec{E} \bullet d\vec{s} = -\frac{\partial}{\partial t} \iint_{A_n} \vec{B} \bullet d\vec{A} \rightarrow Ce = -\frac{\partial}{\partial t} b \tag{6}$$

$$e_i + e_j - e_k - e_l = -\frac{\partial}{\partial t} b_n \tag{7}$$

$$\begin{pmatrix} & \cdots & & \\ 1 & 1 & -1 & -1 \\ & \cdots & & \end{pmatrix} \begin{pmatrix} e_i \\ e_j \\ e_k \\ e_l \end{pmatrix} = -\frac{\partial}{\partial t} \begin{pmatrix} . \\ b_n \\ . \end{pmatrix} \tag{8}$$

In addition to orthogonal hexahedral grids, FIT can also be applied to more general mesh types such as topologically irregular grids and tetrahedral grids, respectively. Figure 1b shows the allocation of the electric voltages and magnetic fluxes on a tetrahedral mesh cell. It is straightforward to derive the corresponding equivalent representation of (7):

$$e_i + e_j - e_k = -\frac{\partial}{\partial t} b_n \tag{9}$$

Applying this scheme to Ampere's law on the dual grid involves the definition of a corresponding discrete curl operator $\tilde{\mathbf{C}}$. Similarly the discretization of the remaining divergence equations introduces discrete divergence operators $\mathbf{S}$ and $\tilde{\mathbf{S}}$, belonging to the primary and dual grid, respectively. As previously indicated, these discrete matrix operators just consist of elements '0', '1' and '-1', representing merely topological information. Finally we obtain the complete discretized set of the equations.

$$\mathbf{C}\hat{\mathbf{e}} = -\frac{d}{dt}\hat{\tilde{\mathbf{b}}} \tag{10}$$

$$\tilde{\mathbf{C}}\hat{\mathbf{h}} = \frac{d}{dt}\hat{\tilde{\mathbf{d}}} + \hat{\tilde{\mathbf{j}}} \tag{11}$$

$$\mathbf{S}\hat{\tilde{\mathbf{b}}} = \mathbf{0} \tag{12}$$

$$\tilde{\mathbf{S}}\hat{\tilde{\mathbf{d}}} = \mathbf{q} \tag{13}$$

In these equations $\hat{\mathbf{e}}$ and $\hat{\mathbf{h}}$ denote the electric fields between grid points and the magnetic fields between dual grid points, respectively.

Vectors $\hat{\tilde{\mathbf{d}}}$, $\hat{\tilde{\mathbf{b}}}$ and $\hat{\tilde{\mathbf{j}}}$ are fluxes over the grid or dual grid faces. In (13) $\mathbf{q}$ represents the electric charges. Due to the consistent transformation, analytical properties of the fields are maintained resulting in corresponding discrete topological operators on the staggered grid.

It should be mentioned that no additional error has yet been introduced and this essential point of FIT discretization is reflected in the fact that important properties of the continuous gradient, curl and divergence operators are still maintained in grid space.

The spatial discretization of a numerical algorithm could cause long term instability, however, it can be shown [1] that the FIT formulation is not affected by such problems, since the set of equations

maintain energy and charge conservation.The discrete analogue of the coupling between fields and fluxes is represented by the material diagonal matrices $\mathbf{M}_E$, $\mathbf{M}_H$ and $\mathbf{M}_\kappa$

$$\hat{\tilde{\mathbf{d}}} = \mathbf{M}_E \hat{\mathbf{e}} \tag{14}$$

$$\hat{\mathbf{h}} = \mathbf{M}_H \hat{\tilde{\mathbf{b}}} \tag{15}$$

$$\hat{\tilde{\mathbf{j}}} = \mathbf{M}_K \hat{\mathbf{e}} + \hat{\tilde{\mathbf{j}}}_A \tag{16}$$

The absorbing boundary conditions of the calculation domain are implemented as a perfectly matched layer (PML). Whereas the classical FDTD has the disadvantage of the staircase approximation of complex boundaries, the Perfect Boundary Approximation (PBA) [3], Thin Sheet Technique (TST), and the Multilevel Subgridding Scheme (MSS), applied in conjunction with FIT maintain all the advantages of the structured Cartesian grids, i.e. high memory efficiency and simulation speed, while allowing an accurate modeling of curved boundaries and fine details with a provable better convergence than the staircase approximation.[1] The discretization of the time derivative is formulated as an explicit algorithm, in leap-frog form. For the lossless case, the integration scheme is described by the following two equations and graphically illustrated in Figure 2.

$$\hat{\mathbf{h}}^{(m+1)} = \hat{\mathbf{h}}^{(m)} - \Delta t \mathbf{M}_H \mathbf{C} \hat{\mathbf{e}}^{(m+1/2)} \tag{17}$$

$$\hat{e}^{(m+3/2)} = \hat{e}^{(m+1/2)} + \Delta t M_E^{-1} \left(\tilde{C} \hat{h}^{(m+1)} - \hat{\tilde{j}}^{(m+1)} \right) \tag{18}$$

The marching-on-time requires in this case only one matrix-vector multiplication, therefore reducing the computational resources ((10) – (13)).

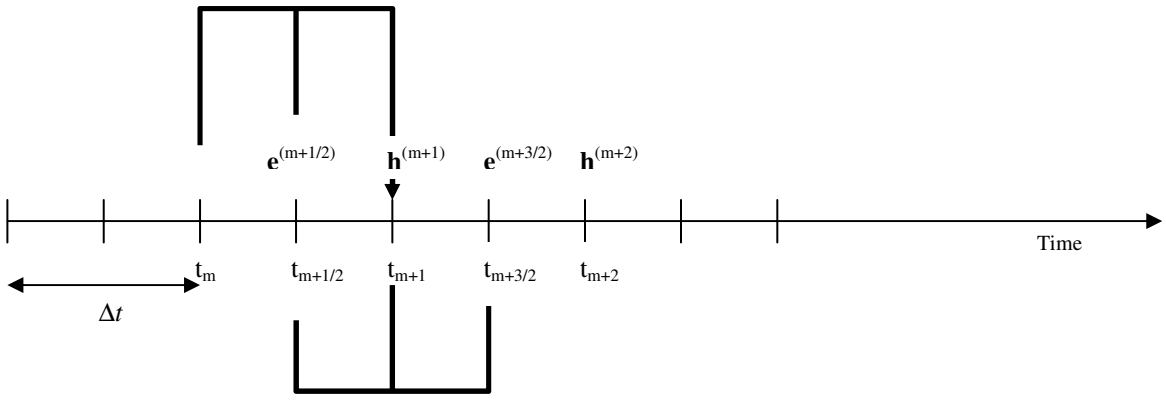

Figure 2 - The leap-frog scheme

[1] CST STUDIO SUITE 2006B™, Perfect Boundary Approximation (PBA) ®, Thin Sheet Technique (TST) ™ and Multilevel Subgridding Scheme (MSS) ™ are trademarks or registered trademarks of CST GmbH, Germany.

This time stepping scheme coincides with the well-known FDTD-algorithm by Yee [4], which was originally derived for uniform Cartesian grids with discrete electric and magnetic field intensities instead of fluxes and voltages.
Since the FDTD scheme is an explicit time marching scheme, it has to full fill the Courant-Friedrich-Levi (CFL) criterion for a maximum stable time step length:

$$\Delta t < \frac{1}{c\sqrt{\frac{1}{\Delta x^2}+\frac{1}{\Delta y^2}+\frac{1}{\Delta z^2}}} \tag{19}$$

which is here given for a three-dimensional Cartesian grid taking into account a possible non-homogeneous material distribution within a cell complex with non-uniform grid spacing.
To briefly summarize, FIT (in time domain) is a discretization method which transforms Maxwell's equations onto a dual grid cell complex, resulting in a set of discrete matrix equations. The degrees of freedom collected in the vectors of this discretization scheme, typically consist in physically measurable, integral quantities such as voltages, currents or charges.

This discretization approach results in sparse integer matrices, $\mathbf{C}$, $\tilde{\mathbf{C}}$, $\mathbf{S}$ and $\tilde{\mathbf{S}}$ which only contains information on the incidence relations of the dual cell complex. This mere restriction to topological information of the grid is responsible for the typical complex property $\mathbf{SC} = \mathbf{0}$ and $\tilde{\mathbf{S}}\,\tilde{\mathbf{C}} = \mathbf{0}$. In connection with the relation $\mathbf{C} = \tilde{\mathbf{C}}^{\mathbf{T}}$ due to duality of the grid pair and with symmetric and positive definite material matrices $\mathbf{D}_{\varepsilon}$ and $\mathbf{D}_{\mu}$ the relations of these incidence matrices allow to prove energy and charge conservation of the spatially discretized equations.

3. FIT applications

3.1 Photonic bandgap structure

Photonic bandgap (PBG) structures [5] are periodic structure in which propagation of certain bands of frequencies is prohibited. Original PBG research was done in the optical region, but PBG properties are scalable and applicable to a wide range of frequencies.
In the last few years there has been an increasing interest in microwave and millimiter-wave application PBG structures. PBG can be achieved by using metallic, dielectric, ferromagnetic or ferroelectric implants.
Figure 3 illustrates a typical PBG structure realized with a two dimensional (2D) square lattice with circles etched in the ground plane.
A 50 ohm mender line runs over the etched ground plane from one side to the substrate to the other and scattering parameters (S-parameters) are calculated by means of FIT and compared with measured results (see Figure 4). The frequency range is 0-6GHz and a good agreement can be observed for both S_{11} and S_{21} magnitude.

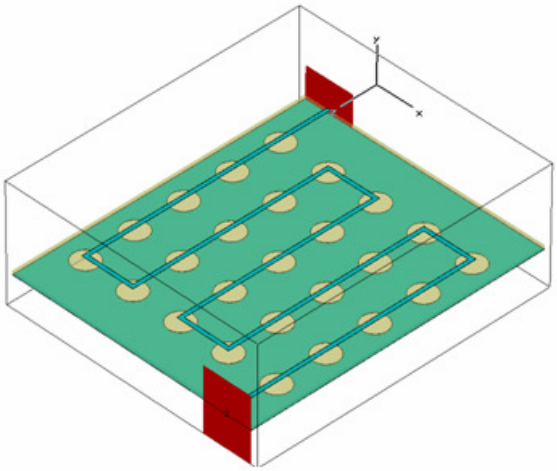

Figure 3 - PBG structure

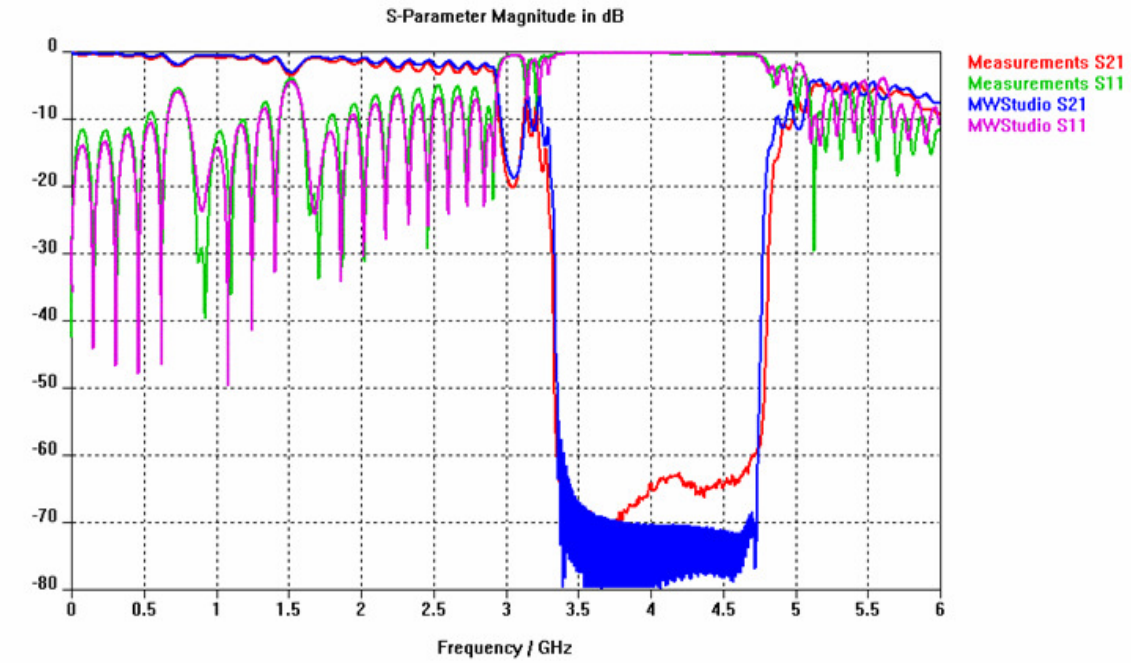

Figure 4 - S-parameters results (S_{11}, S_{12}): comparison between measured and simulated FIT (MWStudio) results.

3.2 Design of EBG structures

Simultaneous switching noise (SSN) or ground bounce noise (GBN) is one of the major concerns for the high-speed digital computer systems with fast edge rates, high clock frequencies, and low voltage levels.

The resonance modes between the power and ground (PWR/GND) planes excited by the SSN causes significant SI problems and EMI issues for the high-speed circuits, therefore the elimination of this noise is essential.
Adding decoupling capacitors to create a low impedance path between PWR/GND planes is a typical way to suppress SSN. However, in general, these capacitors are not effective at frequencies higher than 600 MHz due to their finite lead inductance.
The embedded capacitance with a very thin dielectric is another possible solution to suppress SSN; nevertheless the electromagnetic waves still propagate between the planes with resonance at specific frequencies. A hybrid method which is considered to be an alternative to the use of decoupling capacitors is represented by virtual island (or gapped planes) and shorting vias.
The shorting vias are used to provide the return current path with low impedance and the virtual islands are used to block the PPW noise propagation through PWR/GND plane pairs; even with this methodology the noise suppression is only possible for very narrow band frequency ranges.
Recently, a new idea for eliminating the SSN is proposed by designing EBG structures [6-8]. When inserting an EBG structure in the parallel-plate waveguide-like structure of the Power Distribution Network (PDN) of a Printed Circuit Board (PCB), a resonant circuit composed of the top plate, a single patch, the corresponding via and the plane that connects the vias together is created.
This circuit provides a low-impedance path to high-frequency currents in the PWR planes suppressing propagation within specific frequency ranges.
There are a few primary closed form formulas for describing properties of EBG periodic structures using lumped elements model when the structure is small enough compared to wavelength: the parallel LC resonator which acts like a band stop filter is one of them.
Other models are also available in literature, but to the best of our knowledge there is no exact or even reasonably accurate closed formula that relates the geometrical parameters of the EBGs to the frequency of band stop.
Therefore, and until a highly accurate closed form expression is developed, the effective band of an EBG structure needs to be generated directly or indirectly using numerical simulation tools.
When using numerical codes to extract the effective band of these structures, several techniques are available, but two methods are commonly used: 1) direct method and 2) indirect method.
In the first one the S-parameter between two ports placed across the EBG structures (S_{21}) is evaluated, while in the second one the so-called dispersion diagram is calculated.
Such diagram describes the propagation characteristics of an infinitely periodic structure composed of EBG patches.

3.2.1 Direct method

Figure 5 represents the top view and the stack up of a standard PCB with EBG structure consisting on squared patches.
The outline of entire structure is 80 by 80 mm and the EBG patch layer has 8x8 square patches. The other parameters are: H_1=0.25 mm, H_2=1 mm, d=1mm and l=9mm.
The behavior of the structure is probed at three ports: Port 1, Port 2, and Port 3, as illustrated in the figure. For comparison, a solid plane pair with the same dimensions but without the EBG patch layer is studied as well. The simulated and measured transmission coefficients are shown in the same figure. The band gap region is well defined in both simulation and measured data and a good agreement is observed over the all frequency range.

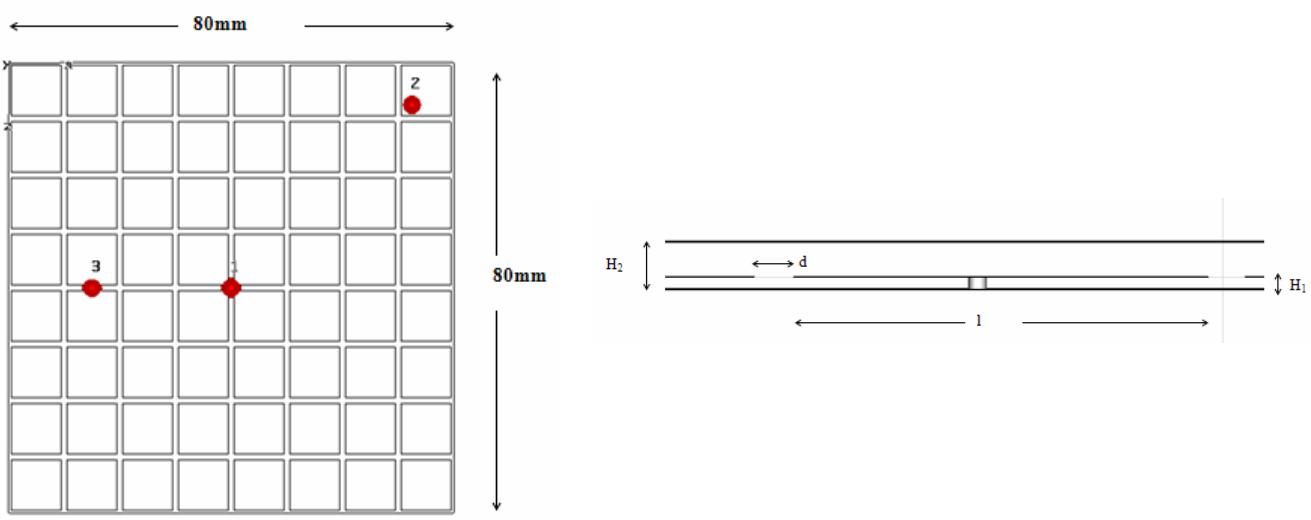

(a)

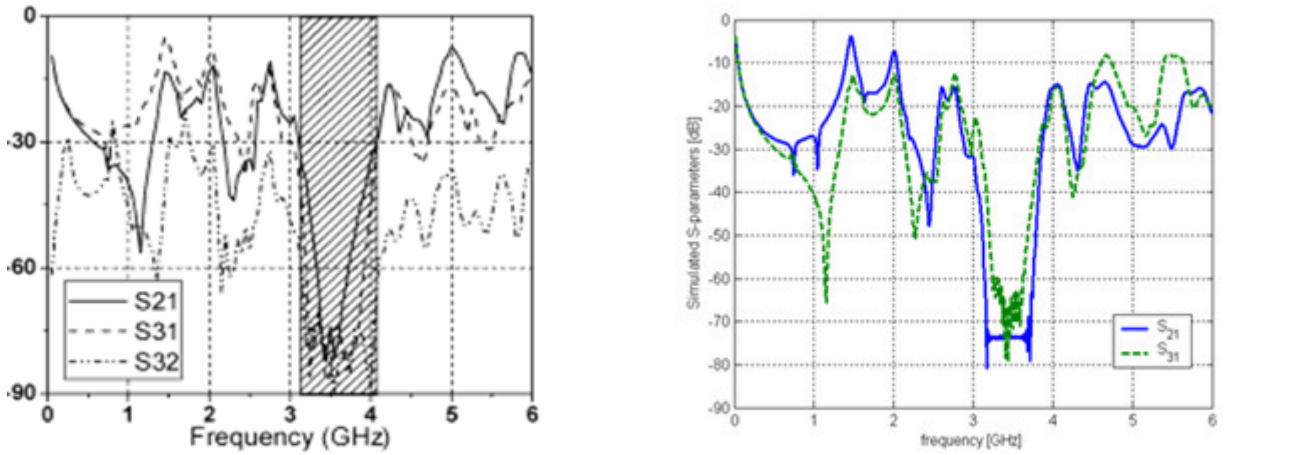

(b)

Figure 5 a): EBG model, top view and cross section, b): S-parameters results (S_{21}, S_{31}): comparison between measured and simulated FIT results.

3.2.2 Indirect method

The indirect method consists on the evaluation of dispersion diagrams which represent propagating modes and band gaps that can potentially exist between such modes. This kind of analysis can be performed by means of eigenmode solver and periodic boundary conditions with phase shift (scan angle) parameterized.

Figure 6 illustrates a typical unit cell and the settings used for the boundary conditions in the full wave simulation. The results are reported in Figure 7, which illustrates the dispersion diagram (with in evidence the band gaps between modes) for the structure presented in Figure 5.

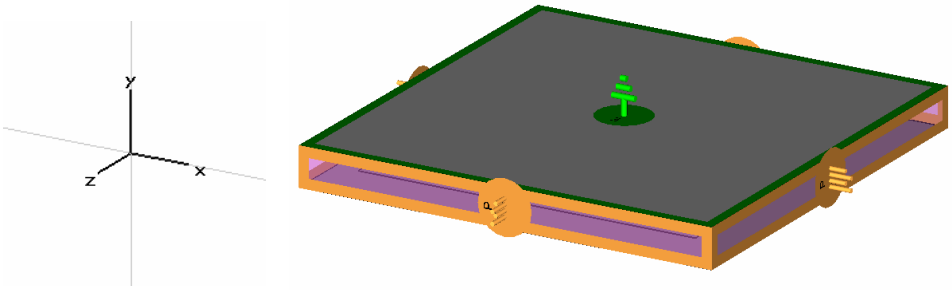

(a)

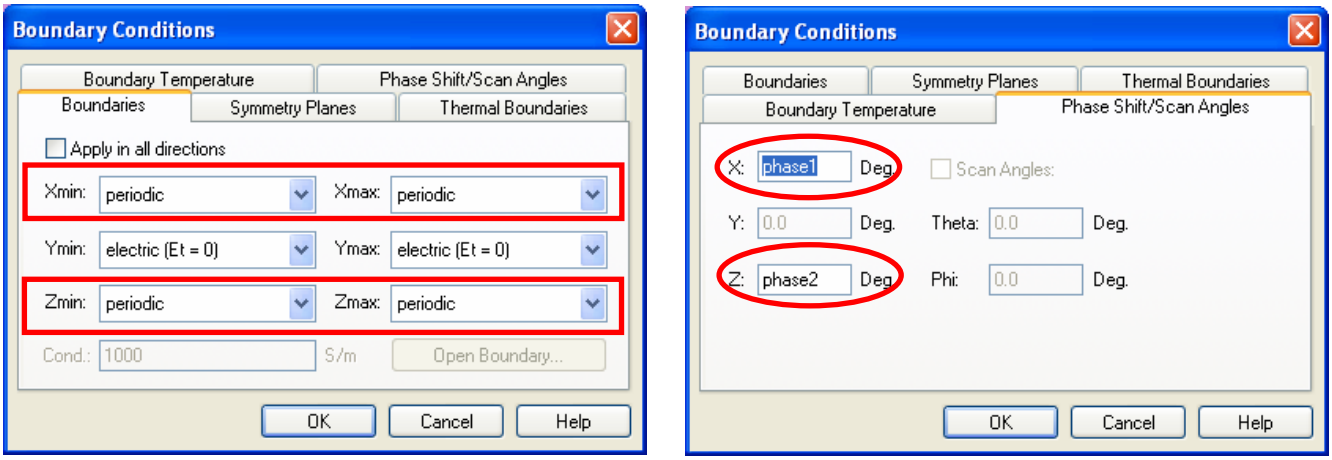

(b)

Figure 6 – a): Unit cell mode and b): periodic boundary conditions definition

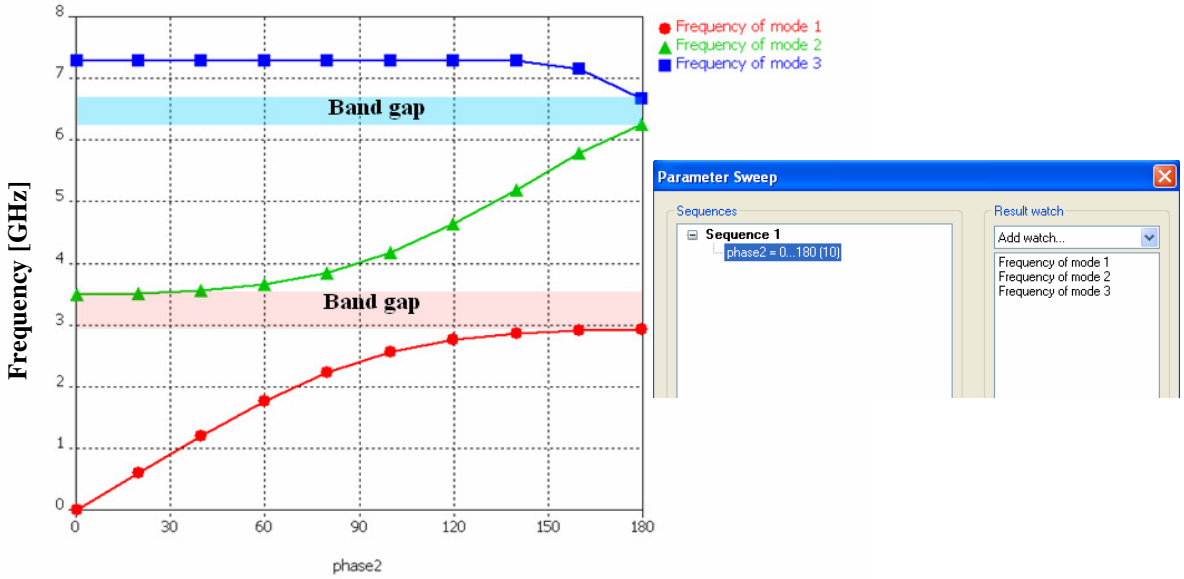

Figure 7 - Dispersion diagram.

One of the main concerns of using EBG structures for SSN noise suppression is related to their cost, which can be very high. For this reason during the last few years 2D EBG structures have been proposed and extensively used for ultra wide band (UWB) noise mitigation and mixed-signal systems.
For example Figure 8a represents a test board used to analyze the performance of the two different EBG structures, it is a 9.15x4.15cm board with FR4 dielectric (ε_r=4.4 and tangδ=0.02 at 0.5GHz).
The EBG layer [11] is characterized by square patches with edge d=1.4mm and double L branches; the parameters are listed in TABLE II.
The S-parameters are reported in the same figure, where a direct comparison between time and frequency domain FIT solver is provided.
Figure 8b represents another possible design of the metal patches [9-10] for the same test board and it consists in two connected simple metal branches.

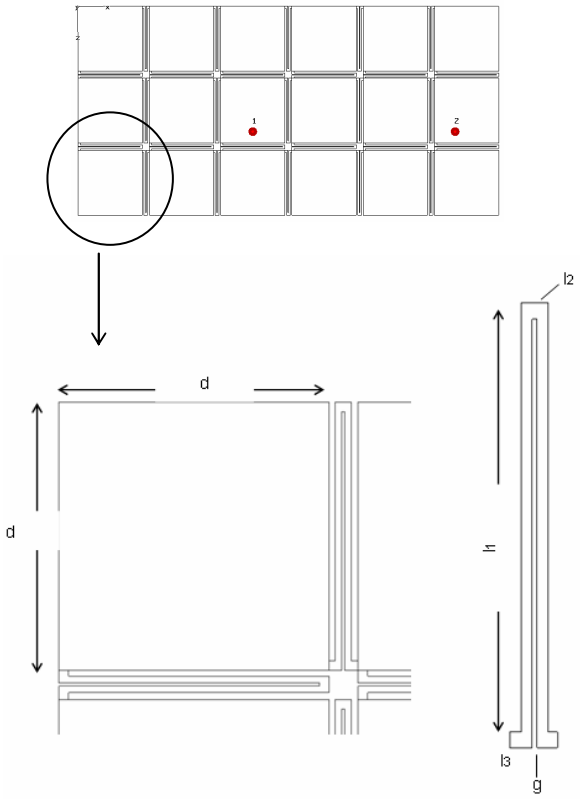

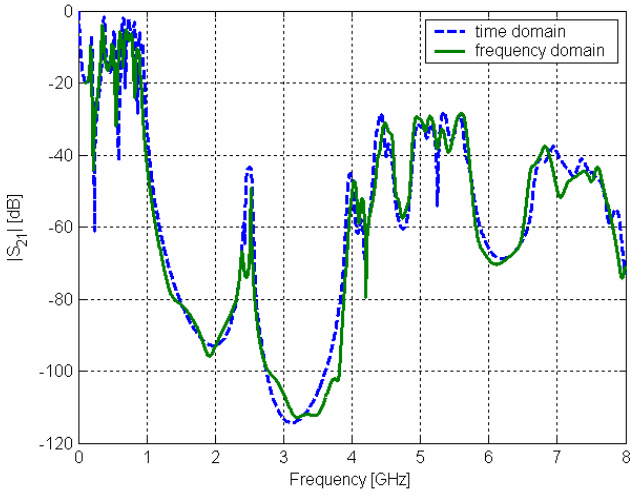

(a)

parameters	d	l_1	l_2	l_3	g
[cm]	1.4	1.35	0.085	0.095	0.055

TABLE II – EBG CELL DIMENSIONS

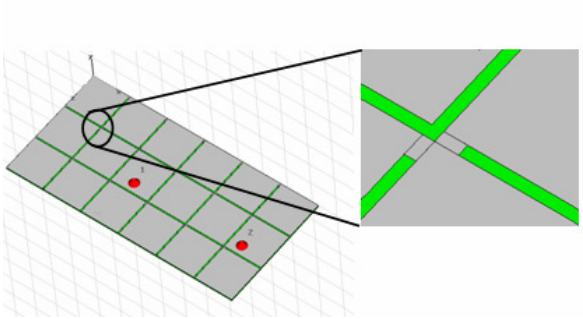

(b)

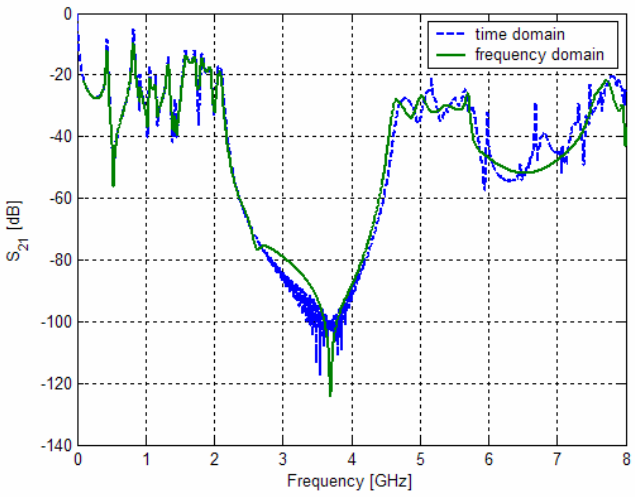

Figure 8 – 2D alternative EBG structures, S_{21}: comparison between time domain (TD) and frequency domain (FD).

Figure 9 illustrates the surface current distribution at different frequencies for the board with continuous PWR plane and the board with EBG structure (Figure 8a).
The current variation is represented by a color contrast in these figures and the unit in the color bars is in [A]. Isolation is of course desirable between the two ports 2 in this example. Figure 9a shows that the EBG structure does not provide good isolation at 500 MHz since this frequency is still in the pass band region. Figure 9b shows the current distribution on the EBG structure at 3.5 GHz, which is a frequency value in the stop band region. The noise generated by the current source on the input port can not propagate to the other metal patches characterizing the EBG structure which means that eventual noise generated by digital circuits can not propagate to the RF circuits located at the output port 2. It should be also noted that the scale for the surface current distribution in Figure 9a, b is reduced to 0-10 [A/m] in order to better visualize the surface current pattern around the input port.

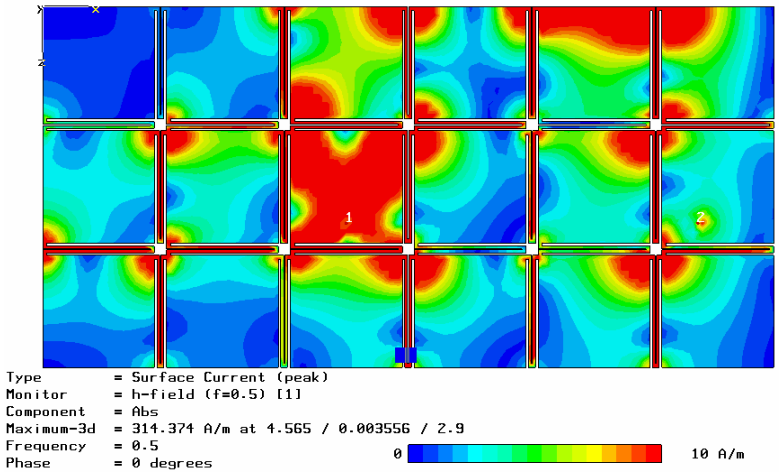

(a)

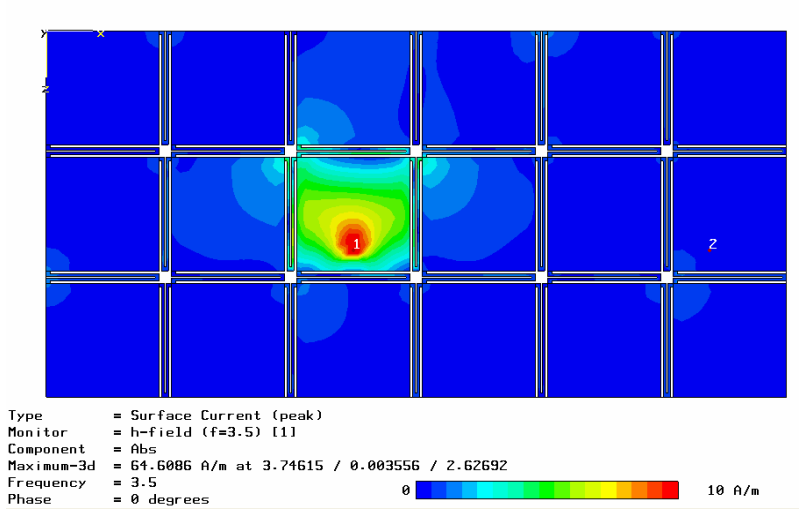

(b)

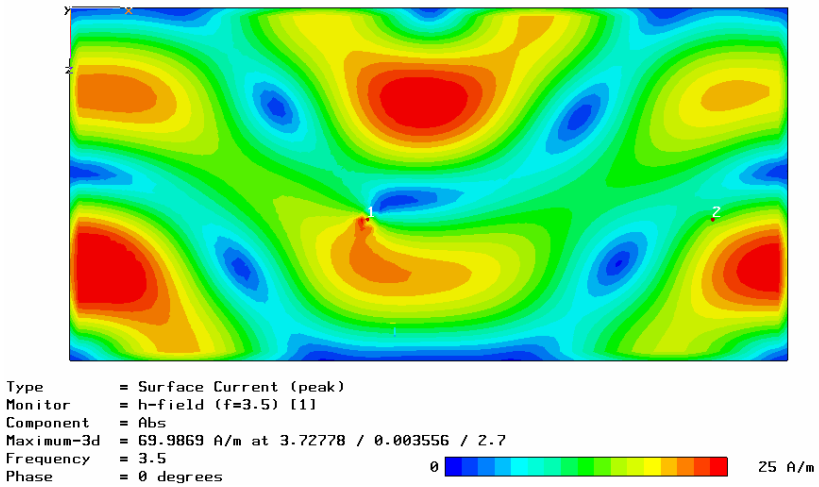

(c)

Figure 9 - Surface current distribution at (a): 0.5GHz on EBG plane, (b): 3.5GHz on EBG plane and (b) 3.5GHz on continuous reference plane

3.3 Stripline and SMA connectors in multilayer stack up structure

At bitrates above one Gb/s the effects of boards' discontinuities on the integrity of the signals can not be neglected. For a correct design, the effects of parasitic, packaging, boards' materials and traces' geometries must be characterized and quantified. An essential step in this process of characterization is the measurement of the properties of the board in terms of S-parameters, input impedance, noise voltage, etc. [12]. Microstrip and stripline structures can not be connected directly to the coaxial ports of a network analyzer (NA).

The structure or device under test must be physically connected to the NA by some kind of transition network or fixture. One of the most frequently used fixture or connector for this kind of applications is the surface mounted adapter (SMA) [13-14].
From engineering point of view the interesting properties of an SMA connector, and hence, the equivalent circuit able to predict those properties, are those of an SMA mounted on a board and not simply isolated.
Because of this it has been chosen to characterize two SMA connected to a stripline (1859mils long), according to the multi-layers stack-up illustrated in Figure 10.

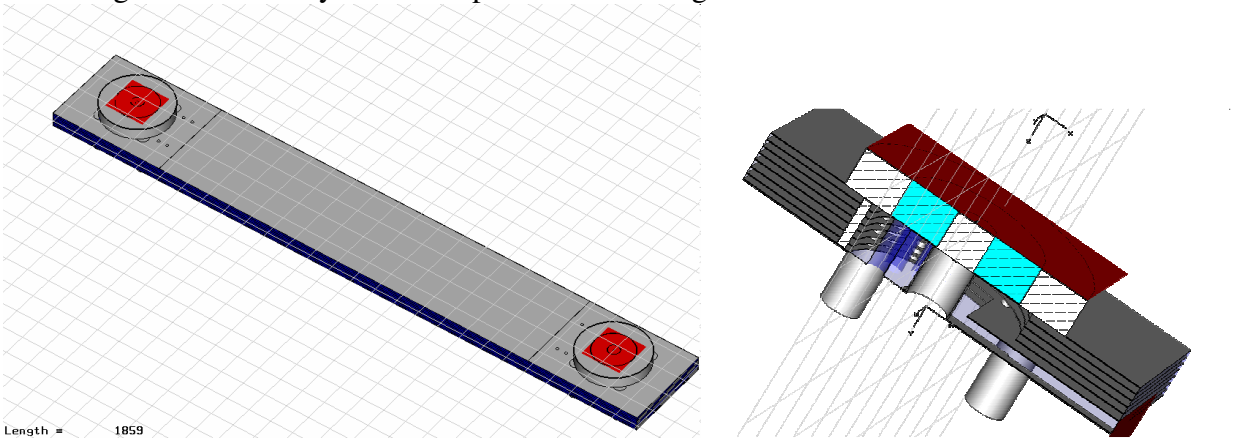

Figure 10 – 3D view of the simulated structure and SMA connector

Figure 11 illustrates the results due to the 3D FIT simulation and the comparison with the measured results: the frequency range is from few MHz up to 20GHz and how it is possible to see a good accuracy is achieved.

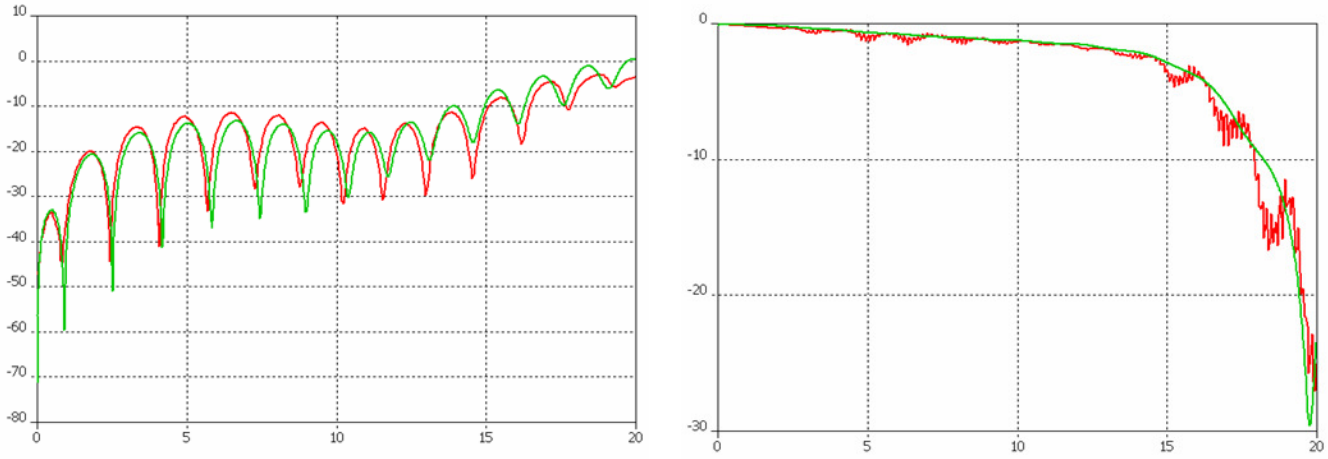

(a) (b)

Figure 11 – Comparison between simulated and measured results, a): $|S_{11}|$, b): $|S_{12}|$

3.4 Advanced Modeling and Measurement of Wideband Horn Antennas

Dual-ridge horn antennas are commonly used as wideband gain standards for antenna measurements. The horn is characterized by connectors and essentially is open with only flared ridge waveguide with lateral bars. It is designed to harmonize the gain with the frequency curve.
At low frequencies the bars appear as a closed surface and increase the bore sight gain of the horn, whereas at high frequencies the bars are electrically transparent and the effective gain decreases.

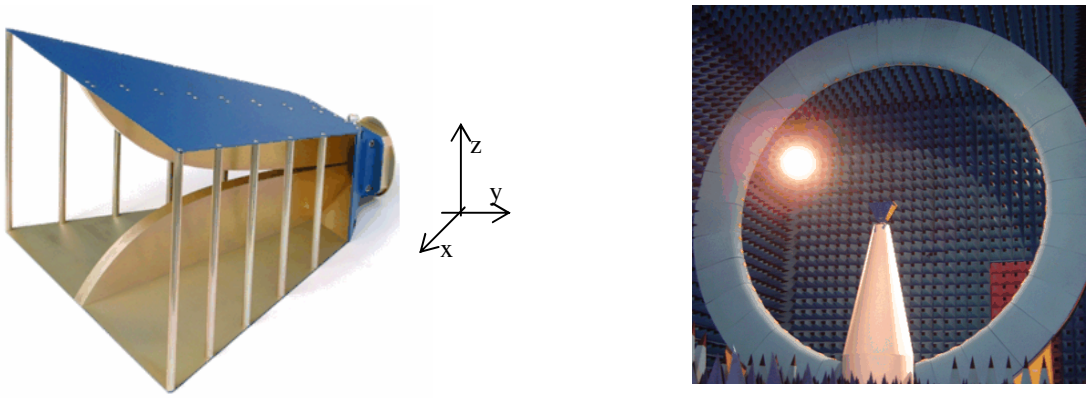

Figure 12 – 3D view of the simulated horn antenna and anechoic chamber used to perform measurements.

The antenna is modeled and simulated with the FIT code by using magnetic symmetry condition in the xz-plane of the antenna and a rather coarse regular mesh with λ/10 spacing.
The used connectors are approximated with simple structures, and dielectric materials are ignored. For the calculations, PEC is assumed for the metallic parts, and PML (Perfect Matching Layer) absorbing boundary conditions are used. The required CPU time for a full analysis is approximately four hours on a Pentium 4, 3 GHz PC.
The dual ridge horn was measured in the Satimo Stargate facility in Atlanta, USA over a frequency range of 800 MHz to 6 GHz. The simulated and measured antenna return loss performance for both amplitude and phase components at the antenna reference port is in good agreement as shown in Figure 13

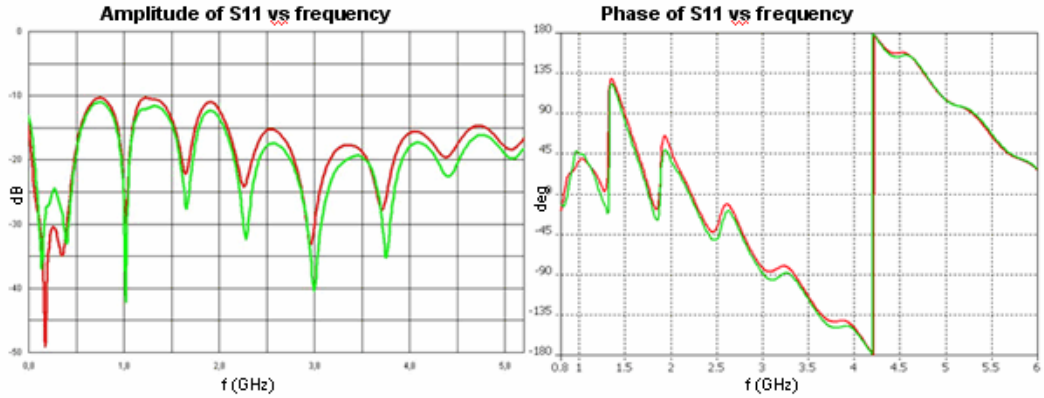

Figure 13 - Simulated with FIT and measured return loss as a function of frequency.

The results of simulated and measured bore sight directivity are plotted in Figure 14. Even in this case as excellent correlation between the two curves can be observed, and the differences fall within the measurement accuracy of the measurement equipment.

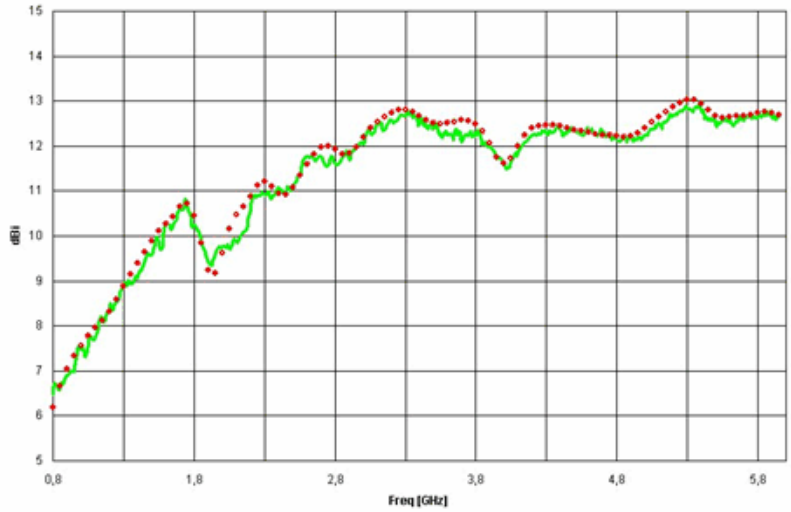

Figure 14 - Simulated with FIT and measured bore sight directivity.

Figure 15 instead shows the comparison of simulated and measured E and H plane radiation patterns at 3.6 GHz. The polarization definition is Ludwig III and it can be seen that the two curves are very close to each other.

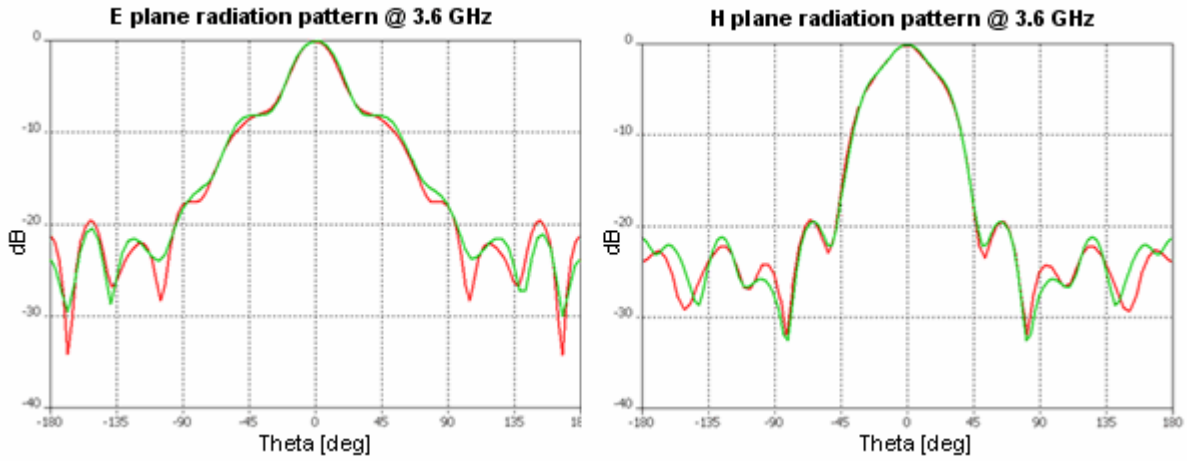

Figure 15 - Simulated and measured E and H plane patterns at 3.6 GHz

The antenna's back radiated fields are often very difficult to determine with high accuracy due to coupling between the antenna under test and the antenna positioner.
The SATIMO Stargate spherical near field system uses a Styrofoam positioner specifically designed for minimum interference with the antenna under test.

The good agreement between the predicted and measured results for the radiated back lobe of the antenna confirms the measurement accuracy in this difficult region.

4. Method of Moment (MoM) and MLFMM enhancement

The method of moments is perhaps the most well known of all computational methods due to its rich history and its widespread application in the analysis of antennas and scatterers. This technique, which was popularized by Harrington in 1967, solves complex integral equations by reducing them to a system of linear equations [15].
The equation solved by the moment method is derived from Maxwell's equations by considering the problem of a field scattered by a perfect conductor (or lossy dielectric).
This equation solved by the MoM is either the magnetic field integral equation (MFIE) or the electric field integral equation (EFIE). The derivation of these starts from the differential form of the time independent Maxwell's equations, where, for linear field qualities:

$$\begin{aligned} \nabla \times \vec{H} &= \vec{J} + i\omega\varepsilon\vec{E} \\ \nabla \times \vec{E} &= -i\omega\mu\vec{H} \\ \nabla \cdot \vec{E} &= \rho / \varepsilon \\ \nabla \cdot \vec{H} &= 0 \end{aligned} \tag{M.1}$$

and $\vec{H}, \vec{E}$ and $\vec{J}$ are vector phasors.

If a volume density of charge and a volume density of current are specified by the continuity condition

$$\nabla \cdot \vec{J} = \frac{-\partial\rho}{\partial t} \tag{M.2}$$

it can be shown that there exists a pair of potential functions ($\vec{A}, \Phi$),which satisfy a certain differential pair (shown in [16]) and which gives the electromagnetic field:

$$\begin{aligned} \vec{B} &= \nabla \times \vec{A} \\ \vec{E} &= -\nabla\Phi - \frac{\partial\vec{A}}{\partial t} \end{aligned} \tag{M.3}$$

Furthermore, by using the gauge transformation, the inhomogeneous Helmholtz equations are derived through substitution of the potential functions into Maxwell's equations; these now equate the volume current to the potential functions.

$$\begin{aligned} (\Delta + \gamma^2)\vec{A} &= -\mu\vec{J} \\ (\Delta + \gamma^2)\Phi &= -\rho / \varepsilon \end{aligned} \tag{M.4}$$

where $\gamma = \omega^2 \varepsilon \mu$ and they satisfy the Lorentz condition

$$\nabla \cdot \vec{A} + \frac{1}{c^2} \frac{\partial \Phi}{\partial t} = 0 \tag{M.5}$$

For the method of moment formulation, the potential functions can be written as [17-18]:

$$\begin{aligned} \vec{A}(\vec{r}) &= \mu \int_V \vec{J}(\vec{r}\,') g(\vec{r}, \vec{r}\,') dV' \\ \Phi(\vec{r}) &= \varepsilon \int_V \rho(\vec{r}\,') g(\vec{r}, \vec{r}\,') dV' \end{aligned} \tag{M.6}$$

Where $g(\vec{r}, \vec{r}\,')$ is the scalar free-space Green's function given by: $\frac{e^{-jk_0|\vec{r}-\vec{r}\,'|}}{4\pi|\vec{r}-\vec{r}\,'|}$. By using the potential functions defined in (M.3), the electromagnetic fields due to surface currents on a sheet can be obtained as

$$\begin{aligned} \vec{H}(\vec{r}) &= -\int_S \vec{J}_s(\vec{r}\,') \times \nabla g(\vec{r}, \vec{r}\,') dS' \\ \vec{E}(\vec{r}) &= -i\omega\mu \int_S [g(\vec{r}, \vec{r}\,') \vec{J}_s(\vec{r}\,') + \gamma^{-2} \nabla g(\vec{r}, \vec{r}\,') \nabla' \cdot \vec{J}_s(\vec{r}\,')] dS' \end{aligned} \tag{M.7}$$

where $\vec{J}_s$ is the sum of the surface currents on both sides of the sheet and ∇' indicates that the differentiation occurs in the source coordinates.
In many practical applications however, the electric and magnetic fields are known and the current distribution is unknown. Since Maxwell's equations are linear, the fields in (M.7) can be decomposed according to the incident/scattered field formulation:

$$\begin{aligned} \vec{H}_{total} &= \vec{H}_{inc} + \vec{H}_{scat} \\ \vec{E}_{total} &= \vec{E}_{inc} + \vec{E}_{scat} \end{aligned}$$

where the incident field is the field that would exist if the scatterer were absent. It can be shown that the electromagnetic field, which is incident on a scatterer, is given by the Stratton-Chu formula [19], and by imposing the appropriate boundary condition, the EFIE and IFIE can be derived. The interested reader is referred to [19], where the derivation is shown.
For the sake of brevity, these equations will not be shown here; however, they relate the unknown surface currents to the known incident fields, making it appropriate for implementation into the MoM.
The first and one of the most crucial steps in the method of moments is to expand $\vec{J}_s$ as a finite sum of basis functions, such that $\vec{J}_S = \sum_{i=1}^{M} J_i \vec{b}_i$, where $\vec{b}_i$ is the i^{th} basis function and J_i is an unknown coefficient.

A large variety of basis functions exist and it is beyond the scope of this introduction to discuss these. It can be shown that by defining appropriate linearly independent weighting functions, the first equation in (M.7) can be written in matrix form as [20]:

$$[\vec{H}] = [Z][\vec{J}] \tag{M.8}$$

where

$$\begin{aligned} Z_{ij} &= < w_j, f_m(b_i) > \\ \vec{J}_i &= J_i \\ \vec{H}_j &= < w_j, \vec{H}_{inc} > \end{aligned} \tag{M.9}$$

In (M.9), w_j are linearly independent weighting functions and $j = 1, 2, ...M$. M is the number of independent equations that need to be solved and $f_m(b_i)$ is the set of basis functions. In (M.8), $\vec{H}$ contains known incident field quantities, and Z is determined by the geometry, leaving the unknown coefficients of the induced currents J_i as the values to be solved.

The specific implementation of the Method of Moments depends upon the selection of the integral field equation and the selection of the appropriate basis functions.

In the formulation above, the magnetic field integral equation (MFIE) formulation was described, but the (electric field integral equation) EFIE could also have been used.

The fast multipole method (FMM) rests on two identities, which are described in [21] and results in an analytical approximation of the Green's function:

$$\frac{e^{-jk_0|\vec{r}+\vec{d}|}}{|\vec{r}+\vec{d}|} = -\frac{jk_0}{4\pi}\oint_S e^{-j\vec{k}\cdot\vec{d}} T_L(\hat{k}\cdot\hat{r}) d^2\hat{k} \tag{M10}$$

with

$$T_L(\hat{k}\cdot\hat{r}) = \sum_{l=0}^{L} (-j)^l (2l+1) h_l^{(2)}(k_0 r) P_l(\hat{k}\cdot\hat{r}) \tag{M11}$$

There are three aspects to the FMM formulation that are important: firstly, in (M11), $k_0 r$ is pre-computed for various distances and angles and this formulation allows a truncated multipole expansion of the Greens function.

The second aspect of importance is that in FMM the interaction matrix is divided into near and far parts. Near interactions are computed as usual with the MoM and far interactions are evaluated approximately using the formulation in equation (M11). For a more detailed description of exactly how this evaluation is achieved, the reader is referred to [21].

A graphical representation of the steps is shown in Figure 16. In part (a), the standard MoM is applied to the near field interactions. Part (b) shows how the FMM defines near field and far field regions (or groups) and in part (c) a recursive hierarchy of groups is introduced. This is known as the MLFMM.

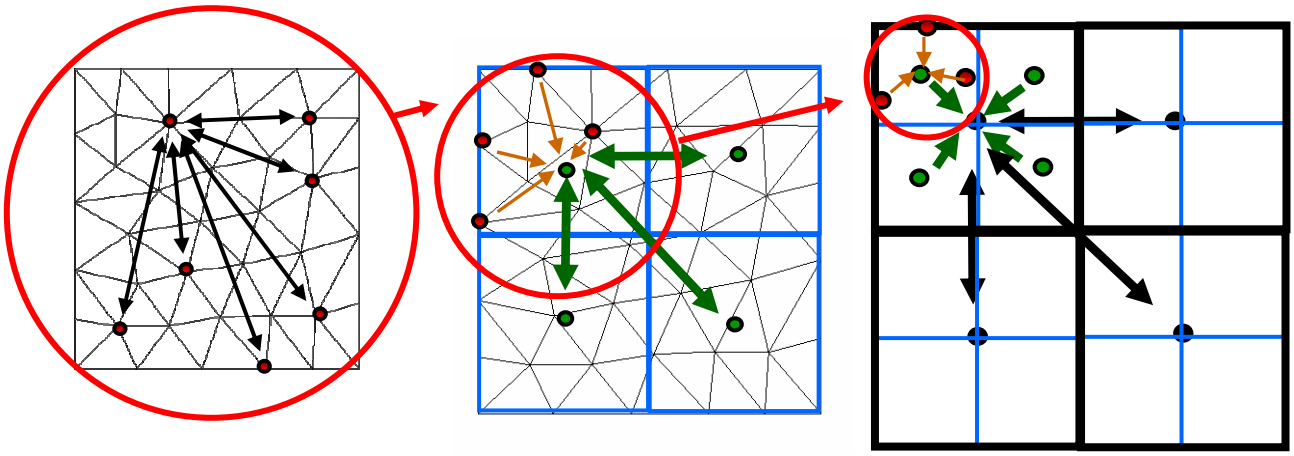

Figure 16 – MLFMM scheme representation.

It is evident from this figure that the MLFMM is very well suited for electrically large structures and for farfield or RCS applications. The MLFMM offers optimal usage of memory and minimal simulation time, while allowing models to be simulated that were previously too large to be analyzed by other numerical methods.

5. MoM applications

In the following sections few examples where the Integral solver, based on the MoM method is used, are illustrated: 1) dielectric sphere and RCS calculation, 2) almond NASA, 3) Apache helicopter.

5.1 Dielectric sphere and RCS calculation

Figure 17 illustrates 1m radius dielectric sphere (ε=1.1, μ=1) excited by means of a plane wave with φ=60, θ=60 degrees. The Integral solver is used to evaluate the RCS at 100MHz on a plane at θ=90 degrees and the numerical results are compared to the analytical solution, according to [22]: a good agreement is observed

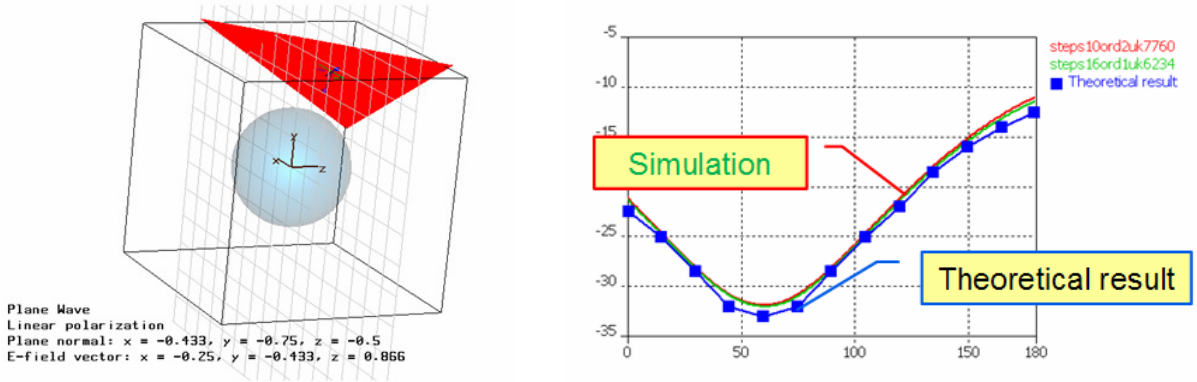

(a) (b)

Figure 17 – a): Dielectric sphere and b): RCS results (dBm) at 100mHz

5.2 Almond NASA

The geometry of the Almond [23] is illustrated in Figure 18: a vertical plane wave excitation is applied and the angle of incidence of the polarized wave is parameterized from 0 to 180 degrees. The Almond is approximately 9.936 inches long and is defined as a PEC, more details can be found in [23].
RCS results at three distinctive frequencies, surface current distribution and Electric field are illustrated respectively in Figure 19 and Figure 20.

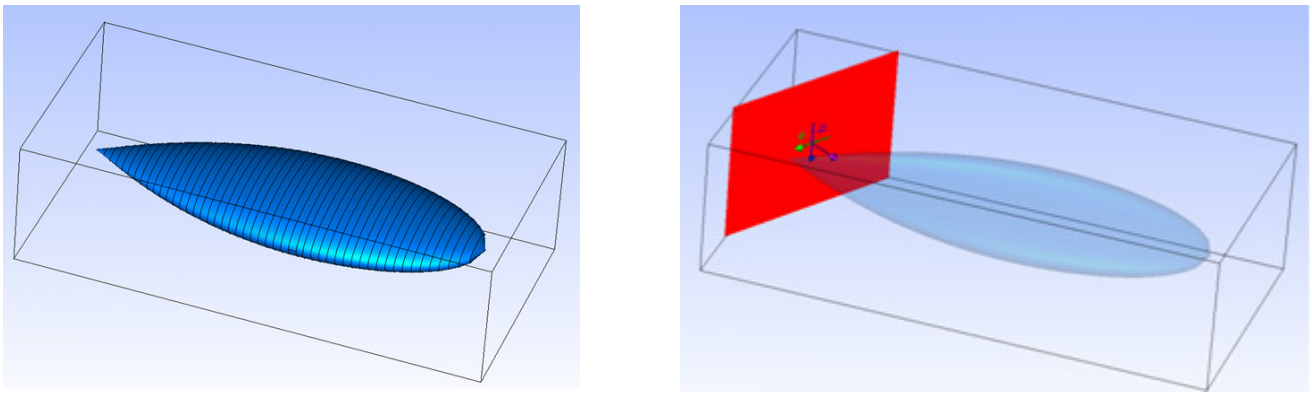

Figure 18– 3D view of the almond NASA and plane wave excitation

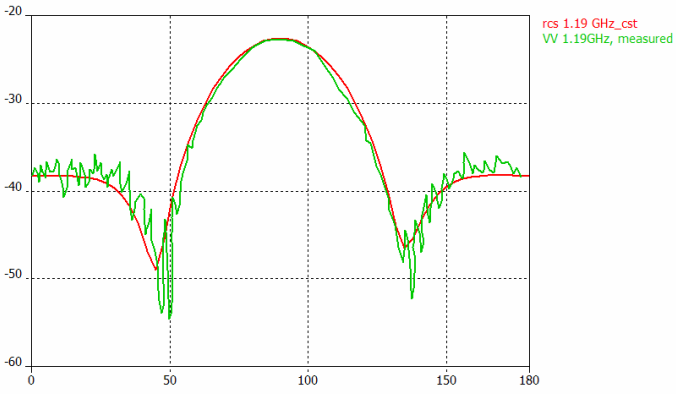

(a)

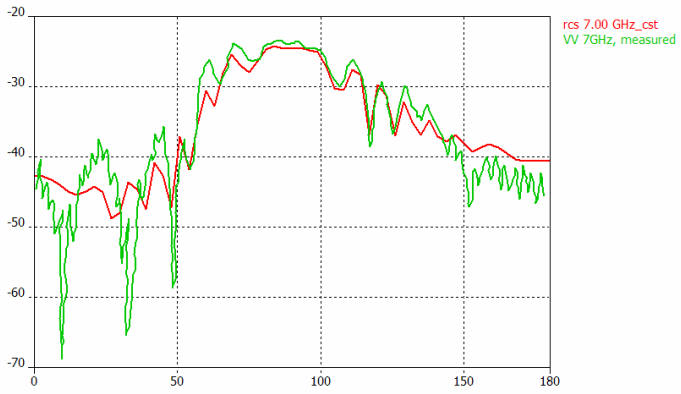

(b)

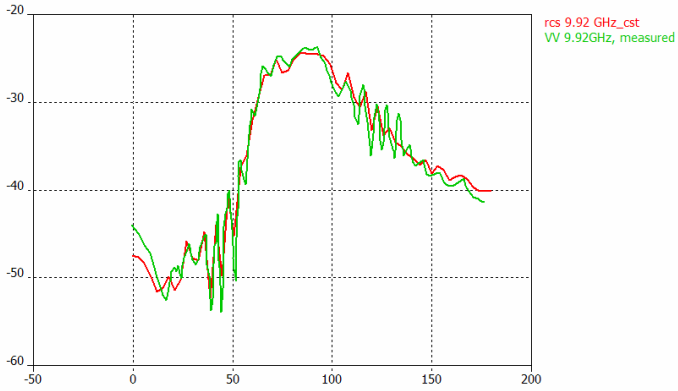

(c)

Figure 19– RCS calculation: comparison between measured and simulated MoM results, a): 1.19GHz b): 7GHz and c): 9.92GHz.

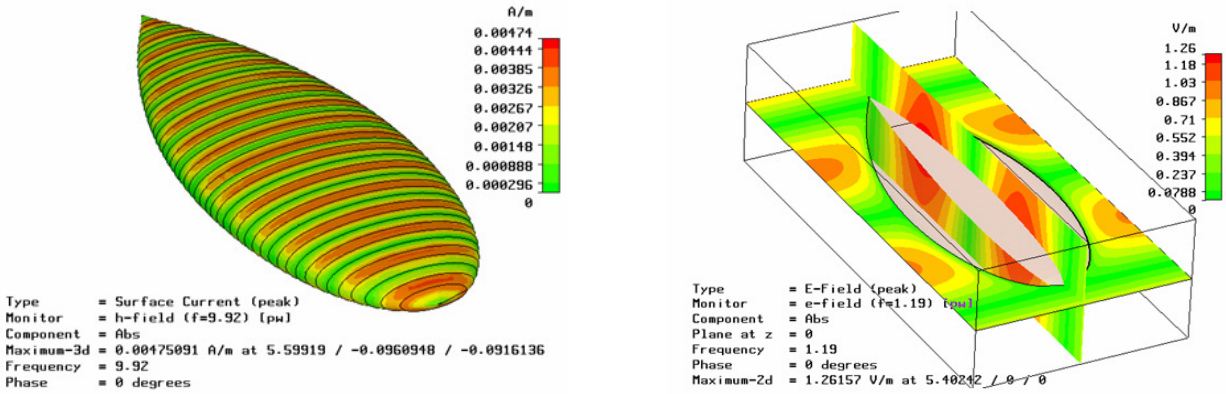

Figure 20 – Surface current distribution and Electric field on two intersecting planes

5.3 RCS and Surface Current calculation for an Apache Helicopter

This example demonstrates the simulation of an electrically large helicopter. The length of the helicopter is about 7.8 meters and, therefore, the aircraft is approximately 180 wavelengths in size. The helicopter is illuminated by a plane wave at 7 GHz and the surface mesh is represented by about 830.000 surface cells. Accordingly, the simulation is performed using more than 1.25 million unknowns.
Figure 21 shows the plane wave illumination of the helicopter at 7 GHz: the electric field vector for the plane wave excitation points into the vertical direction. Figure 22 depicts the surface current distribution over the helicopter at 7GHz

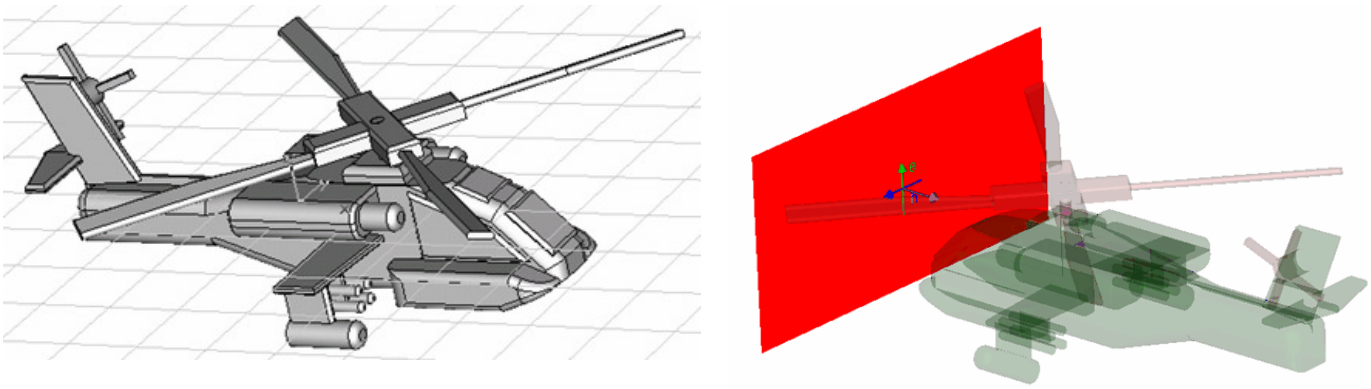

Figure 21 - The geometry of the helicopter and the pane wave excitation

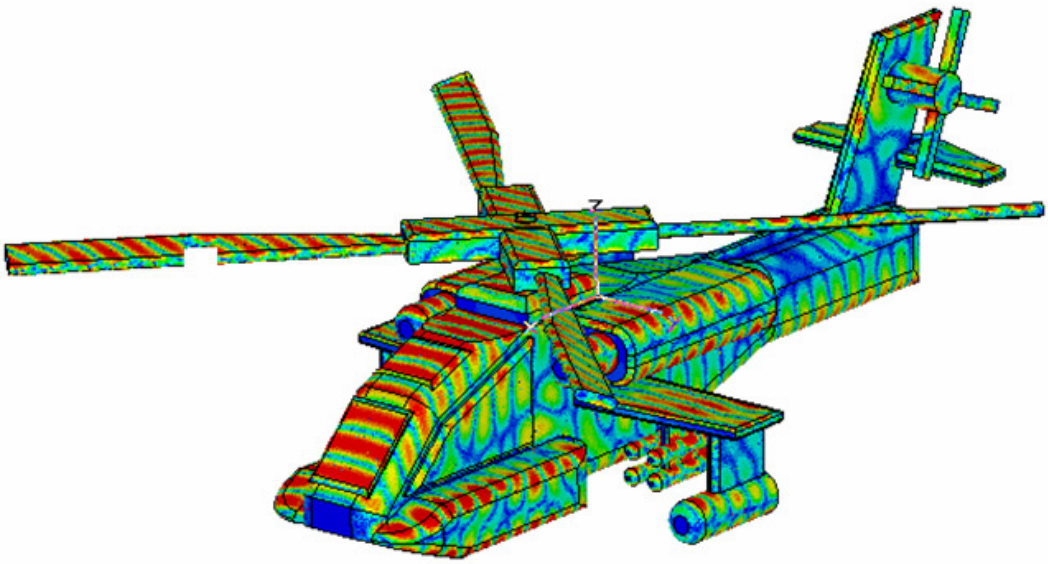

Figure 22- Surface current distribution at 7GHz

6. CONCLUSION

With the proliferation of electromagnetic solvers throughout microwave research and industry, their accuracy is becoming an issue of great practical importance. An overview of FIT and MoM (with the enhancement of MLFMM) numerical methods is presented along with a consistent number of examples covering different field of applications. It is demonstrated how FIT with the time domain solver is well suitable for broadband simulation and for complex geometry due to the non uniform hexahedral mesh enhanced by PBA and TST. Furthermore the possibility to implement FIT in both time and frequency domain allows validating the results by using two complete different mesh types: hexahedral and tetrahedral.
MoM is presented to be very powerful for large structure, in principle dominated by metal, although some results show the accuracy of the method for dielectric problems as well (dielectric sphere). From the present study it appears that FIT is very useful for the solution of a very broad band problem types, while MoM with MLFMM is reserved for more exclusive applications and large models 30-50λ.

Acknowledgments

The authors would like to thanks J. Wang with CST of America for the simulation of the almond NASA and J. Eberhard for the useful discussions on the MoM method and for providing the helicopter model/results.

References

[1] T. Weiland, "A discretization method for the solution of Maxwell's equations for six-component fields", Electronics and Communication, (AEÜ), Vol. 31 (1977), p. 116.

[2] T. Weiland, "Time Domain Electromagnetic Field Computation with Finite Difference Methods", International Journal of Numerical Modelling, Vol. 9, pp. 295-319 (1996).

[3] B. Krietenstein, R. Schuhmann, P. Thoma and T. Weiland, "The Perfect Boundary Approximation technique facing the challenge of high precision field computation", Proc. of the XIX International Linear Accelerator Conference (LINAC'98), Chicago, USA, 1998, pp. 860-862.

[4] K.S. Yee, "Numerical Solution of Initial Boundary Value Problems Involving Maxwell's Equations in Isotropic Media", IEEE, Antennas and Propagation 14, 1966, pp.302-307.

[5] V.Radisic, Y.Qian, R. Coccioli, T. Itoh, "Novel 2-D Photonic Bandgap Structure for Microstrip Lines", IEEE Microwave and Guided Wave Letters, vol.8, n.2, February 1998.

[6] Abhari, G.V. Eleftheriades, "Metallo - dielectric electromagnetic band gap structures for suppression and isolation of parallel-plate noise in high speed circuits", *IEEE Trans. On Microwave Theory and Tech*, vol. 51, no. 6, pp. 1629–1639, June 2003.

[7] G.Chen, K.L.Melde, "Cavity resonance suppression in power delivery systems using electromagnetic band gap structures", IEEE Transaction on Advanced Packaging, vol. 29, no. 1, pp. 21–30, February 2006.

[8] S. Shahparnia, O. M. Ramahi, "Electromagnetic interference (EMI) and reduction from printed circuit boards (PCB) using electromagnetic bandgap structures", *IEEE Trans. Electromagnetic Comp*, vol. 46, no. 4, pp. 580–587, November 2004.

[9] J.Choi, V.Govind, M. Swaminathan, "A novel electromagnetic band gap (EBG) structure for mixed signal system applications", Proc. of *IEEE Radio and Wireless*, Atlanta, Georgia, September 2004.

[10] J.Choi, V. Govind, M. Swaminathan et Al., Noise suppression and isolation in mixed signal systems using alternative impedance electromagnetic bandgap (Al-EBG) structure", accepted for *IEEE Trans. on Electromagnetic Compatibility*.
[11] A.Ciccomancini Scogna, M.Schauer, "A Novel Electromagnetic Bandgap Structure for SSN Suppression in PWR/GND plane pairs", in Proc. of ECTC 2007, Nevada, USA.
[12] S.H.Hall, G. W.Hall, J.A.McCall, *High-Speed Digital System Design – A Handbook of Interconnect Theory and design Practises*, John Wiley & Sons, INC., New York, USA, 2000.R. F. Harrington, *Time-harmonic Electromagnetic Fields*, McGraw-Hill, 1961
[13] K.Naishadham, T. Durak "Measurement-Based Closed-Form Modeling of Surface-Mounted RF Components", *IEEE Trans. Microwave Theory Tech.*, vol. 50, no.10, pp. 2276-2286, October 2002.
[14] G. Antonini, A Ciccomancini Scogna, A. Orlandi, "Equivalent circuit extraction for an SMA connector", in *Proc. of PIERS* 2003, Pisa, Italy.
[15] R.F. Harrington, "Field Computation by Moment Methods", The Macmillan Co., New York, 1968.
[16] G.S. Smith, "An Introduction to Classical Electromagnetic Radiaton", Cambridge: Cambridge University Press, 1997.
[17] Eberhard, J.P. "The Integral Equation Solver", Proceedings of the CST Field Training 2006, Oct. 8th-11th 2006, Darmstadt, Germany.
[18] Davidson, D.B., "Computational Electromagnetics for RF and Microwave Engineering", Cambridge: Cambridge University Press, 2005.
[19] Ishimaru, A., "Electromagnetic Wave Propagation, Radiation, and Scattering", New Yersey: Prentice-Hall, Inc., 1991
[20] Hubing, T.H., "Survey of Numerical Electromagnetic Modeling Techniques" Internal Report nr TR91-1-001.3, University of Missouri-Rolla, 1991 (http://www.emclab.umr.edu/pdf/TR91-1-001.pdf)
[21] Coifman, R, Rokhlin, V and Wandzura, S, "The Fast Multipole Method for the Wave Equation: A Pedestrian Prescription" IEEE Antennas and Propagation Magazine, vol. 35, no. 3, Jun. 1993, pp. 7–12.
[22] R. F. Harrington, *Time-harmonic Electromagnetic Fields*, McGraw-Hill, 1961
[23] Ali E. Yılmaz, J.Ming Jin, E. Michielssen, "Time Domain Adaptive Integral Method for Surface Integral Equations", *IEEE Trans. on Antennas and Propag*., vol.52, n.10, October 2004, pag. 2692-2708.